Elastic regimes of subisostatic athermal fiber networks

A. J. Licup, A. Sharma, and F. C. MacKintosh

Department of Physics and Astronomy, VU University Amsterdam, 1081 HV Amsterdam, The Netherlands

Athermal models of disordered fibrous networks are highly useful for studying the mechanics of elastic networks composed of stiff biopolymers. The underlying network architecture is a key aspect that can affect the elastic properties of these systems, which include rich linear and nonlinear elasticity. Existing computational approaches have focused on both lattice-based and off-lattice networks obtained from the random placement of rods. It is not obvious, *a priori*, whether the two architectures have fundamentally similar or different mechanics. If they are different, it is not clear which of these represents a better model for biological networks. Here, we show that both approaches are essentially equivalent for the same network connectivity, provided the networks are subisostatic with respect to central force interactions. Moreover, for a given subisostatic connectivity, we even find that lattice-based networks in both two and three dimensions exhibit nearly identical nonlinear elastic response. We provide a description of the linear mechanics for both architectures in terms of a scaling function. We also show that the nonlinear regime is dominated by fiber bending and that stiffening originates from the stabilization of subisostatic networks by stress. We propose a generalized relation for this regime in terms of the self-generated normal stresses that develop under deformation. Different network architectures have different susceptibilities to the normal stress but essentially exhibit the same nonlinear mechanics. Such a stiffening mechanism has been shown to successfully capture the nonlinear mechanics of collagen networks.

I. INTRODUCTION

The elastic stress response of living cells and tissues is governed by the viscoelasticity of complex networks of filamentous proteins such as the cytoskeleton and the extracellular matrix [1–9]. This property of such biological gels not only makes living cells and tissues stiff enough to maintain shape and transmit forces under mechanical stress but also provides them the compliance to alter their morphology needed for cell motion and internal reorganization. Unlike ordinary polymer gels and other materials with rubberlike elastic properties, however, biological gels behave nonlinearly in response to deformation. One classic feature is strain stiffening, where a moderately increasing deformation leads to a rapid increase in stress within the material. Such is observed in gels of cytoskeletal and extracellular fibers [6–8,10–19] and in soft human tissues [20]. Another interesting aspect of elastic nonlinearity is the so-called negative normal stress. Most solid materials exhibit what is known as the Poynting effect [21] where the response is to expand in a direction normal to an externally applied shear stress. This effect explains why metal wires increase in length under torsional strain. By contrast, crosslinked biopolymer gels exhibit the opposite response to shear deformation, which can be understood either in terms of the inherent asymmetry in the extension-compression response of thermal semiflexible polymers or nonaffine deformations in athermal fiber networks [22–24].

Research on the elastic properties of fiber networks often aimed to elucidate the microscopic origins of viscoelasticity has generated significant progress, making way for models that highlight the importance and interplay of semiflexible filaments, crosslink connectivity, network geometry, and disorder. An important consideration when modeling the elastic response of biological gels with fiber networks is the inherent instability of the underlying geometry with respect to stretching. Whether intracellular or extracellular

biopolymer networks are studied, the constituent fibers usually form either crosslinked or branched architectures [25–27], corresponding to an average connectivity below the Maxwell isostatic criterion for marginal stability of spring networks with only stretching response. Such systems, however, can be stabilized by a variety of additional interactions, such as fiber bending rigidity [9,28,29], thermal fluctuations [30], internal stresses generated by molecular motors [31,32], boundary stresses [26], or even strain [27,33]. These stabilizing fields give rise to interesting linear and nonlinear elastic behavior.

Detailed analytical and computational work on the linear elastic response of networked systems reveals two distinct regimes: an affine regime dominated by extension or compression of the fibers and a crossover to a nonaffine one dominated by fiber bending [34–37]. In addition to fiber elasticity, these linear regimes are also found to be dictated by network structure and disorder and can exhibit rich zero-temperature critical behavior, including a crossover to a mixed regime [29]. Such linear regimes in turn have important consequences to the nonlinear response where large deformations are involved. In particular, large stresses applied to a network initially dominated by filament bending would lead to a strong strain-induced stiffening response [27], which coincides with the onset of negative normal stress [22,24].

In general, the variety of computational models to understand certain specific aspects of linear or nonlinear network elasticity can either be based on off-lattice [24,34–36,38–40] or lattice structures [29,41–44], which can also be combined with a mean-field approach [29,37,45,46]. Indeed, much has been done with lattices to understand linear elasticity, in contrast to nonlinear elasticity often studied on random networks. The advantage of lattice models is the computational efficiency as well as the relative ease with which one can generate increasingly larger network sizes. We intend to study nonlinear elasticity using a lattice-based model and compare with results on a random network. We begin with a detailed description

of the disordered phantom network used to study the elastic stress response of passive networks with permanent crosslinks [41,42,47]. This model allows independent control of filament rigidity, network geometry and crosslink connectivity. We present our results in the nonlinear elastic regime, focusing on shear stiffening and negative normal stress. Finally we conclude with implications when using lattice-based models to understand nonlinear elasticity of stiff fiber networks.

II. MODELING SUBISOSTATIC ATHERMAL NETWORKS

Biopolymers can form either crosslinked or branched network structures that have average connectivity somewhere between threefold ($z = 3$) at branch points and fourfold ($z = 4$) at crosslinks [25–27]. If these nodes interact only via central forces such as tension or compression of springs, the network rigidity vanishes and the resulting networks are inherently unstable [48]. However, it is known that these subisostatic systems can be stabilized by other effects such as the bending of rigid fibers [28,29,35,49]. In this section, we describe a minimal model of a subisostatic network in which the constituent fibers are modeled as an elastic beam the rigidity of which is governed by pure enthalpic contributions.

A. Network generation

We generate a disordered phantom network [41,42] by arranging fibers into a d-dimensional space-filling regular lattice of size W^d (number of nodes). We use triangular and fcc lattices for $d = 2$ and 3, respectively. The network occupies a total volume [or area for two-dimensional (2D) lattices] $V = v_0 W^d$, where v_0 is the volume (or area) of a unit cell. Periodic boundaries are imposed to reduce edge effects. Freely hinged crosslinks bind the intersections of fiber segments permanently at the vertices, which are separated by a uniform spacing ℓ_0. Since a full lattice has a fixed connectivity of either $z_{max} = 6$ (2D) or $z_{max} = 12$ [three-dimensional (3D)], we randomly detach binary crosslinks (i.e., $z = 4$) at each vertex. Starting from a 2D triangular network, this results in an average distance l_c between crosslinks, where $l_c = 3\ell_0/2$, while $l_c = \ell_0$ for the 3D fcc lattice. In either case, this procedure creates a network with connectivity $z = 4$ composed of *phantom* segments that can move freely and do not interact with other segments, except at crosslinks. Thus far, all fibers span the system size which leads to unphysical stretching contributions to the macroscopic elasticity. We therefore cut at least one bond on each spanning fiber. Finally, to reduce the average connectivity to physical values of $z < 4$, we *dilute* the lattice by cutting random bonds with probability $q = 1 - p$, where p is the probability of an existing bond. Any remaining dangling ends are further removed. The lattice-based network thus generated is subisostatic with average connectivity $2 < z < 4$, average fiber length $L = \ell_0/q$, and average distance between crosslinks $l_c = \ell_0$ for an initial undeformed fcc lattice and $l_c \simeq 1.4\ell_0$ for an initial triangular lattice with $z \simeq 3.2$.

Mikado networks are generated by random deposition of monodisperse fibers of unit length onto a 2D box with an area $W \times W$. A freely hinged crosslink is inserted at every point of intersection resulting in a local connectivity of 4. However, some of the local bonds are dangling ends and are removed

from the network, thus bringing the average connectivity below 4. The deposition continues until the desired average connectivity is obtained.

For the rest of this work, we use l_c to denote the average distance between crosslinks for both lattice-based and Mikado networks. For simplicity and unless otherwise stated, we use $l_c = \ell_0$ for both 2D and 3D lattice-based networks.

B. Fiber elasticity

In modeling fiber networks, each fiber can be considered as an Euler-Bernoulli or Timoshenko beam [40,47]. From a biological perspective, it is important to consider the semiflexible nature of the fibers to account for the finite resistance to both tension and bending. When the network is deformed, any point on every fiber undergoes a displacement which induces a local fractional change in length $\frac{dl}{ds}$ and a local curvature $|\frac{d\hat{t}}{ds}|$. The elastic energy thus stored in the fiber is given by [36]

$$\mathcal{H}_f = \frac{\mu}{2} \int_f \left(\frac{dl}{ds}\right)^2 ds + \frac{\kappa}{2} \int_f \left|\frac{d\hat{t}}{ds}\right|^2 ds, \qquad (1)$$

where the parameters μ and κ describe the one-dimensional Young's (stretch) modulus and bending modulus, respectively. The integration is evaluated along the undistorted fiber contour. The total energy $\mathcal{H} = \sum_f \mathcal{H}_f$ is the sum of Eq. (1) over all fibers.

Treating the fiber as a homogeneous cylindrical elastic rod of radius a and Young's modulus E, we have from classical beam theory [50] $\mu = \pi a^2 E$ and $\kappa = \frac{1}{4}\pi a^4 E$. These parameters can be absorbed into a *bending length scale* $l_b = \sqrt{\kappa/\mu} = a/2$. One can normalize l_b by the geometric length l_c to obtain a dimensionless fiber rigidity $\tilde{\kappa} = (l_b/l_c)^2$, or

$$\tilde{\kappa} = \frac{\kappa}{\mu l_c^2}. \qquad (2)$$

As noted in Sec. II A, for simplicity we take l_c to be the lattice spacing ℓ_0 of the 2D and 3D lattice-based networks. For Mikado networks, l_c is the average spacing between crosslinks.

In our network of straight fibers with discrete segments, a midpoint node is introduced on every segment to capture at least the first bending mode over the smallest length scale l_c. The set of spatial coordinates $\{r_j\}$ of all nodes (i.e., crosslinks, phantom nodes, and midpoints) thus constitutes the internal degrees of freedom of the network. Under any macroscopic deformation, e.g., *simple shear* strain γ, the nodes undergo a displacement $\{r_j\} \to \{r'_j\}$ which induces the dimensionless local deformations $\lambda_j = \delta\ell_j/\ell_j$ and $\theta_j = |\hat{t}_{j,j+1} - \hat{t}_{j-1,j}|$. Here, $\delta\ell_j = \ell'_j - \ell_j$ is the length change of a fiber segment with rest length $\ell_j = |r_{j+1} - r_j|$ and $\hat{t}_{i,j}$ is a unit vector tangent to segment $\langle ij \rangle$. The fiber then stores an elastic energy expressed as a discretized form of Eq. (1):

$$\mathcal{H}_f = \frac{1}{2} \sum_{j \in f} \left(\mu \ell_j \lambda_j^2 + \frac{\kappa}{l_j} \theta_j^2 \right),$$

where $l_j = \frac{1}{2}(\ell_{j-1} + \ell_j)$. By taking $l_j \simeq \ell_j \simeq l_c$, we can rewrite this equation with an explicit dependence on

deformation and fiber rigidity as

$$\mathcal{H}_f(\gamma,\tilde{\kappa}) = \mu l_c \sum_{j \in f} \hat{\mathcal{H}}_j(\gamma,\tilde{\kappa}), \qquad (3)$$

where $\hat{\mathcal{H}}_j = \frac{1}{2}(\lambda_j^2 + \tilde{\kappa}\theta_j^2)$ is a dimensionless elastic energy of a fiber segment. Note that the dependence on $\{\lambda_j,\theta_j\}$ is accounted for by the macroscopic strain γ.

C. Network elasticity

The network elasticity is determined not only by the rigidity of the constituent fibers but also by the network connectivity, which we characterize equivalently by z or the average *crosslinking density* L/l_c, that is also the number of crosslinks per fiber. This ratio has been shown to govern the network's affine or nonaffine response to the applied deformation [35,42]. A higher density of crosslinks leads to a more affine (i.e., uniform) deformation field. By contrast, fewer crosslinks per fiber allows the possibility of exploring nonuniform displacements resulting in a nonaffine response [34,43]. Effectively, the network elasticity can be characterized by $\tilde{\kappa}$ and L/l_c.

The stress and moduli depend on the energy density $\mathcal{U}$, i.e., energy per unit volume. Since the expression for the total energy involves an integral along the contour length of all fibers, $\mathcal{U}$ is naturally proportional to the total length of fiber per unit volume. Thus, ρ, together with the energy per length, μ, set the natural scale for energy density, stress, and modulus. Thus, we write

$$\mathcal{U} = \mu\rho\langle\hat{\mathcal{H}}_j(\gamma,\tilde{\kappa})\rangle_s = \frac{\mu}{l_c^{d-1}}\tilde{\mathcal{U}}(\gamma,\tilde{\kappa}), \qquad (4)$$

where $\langle\cdot\rangle_s$ is an average over all fiber segments. Expressing ρ as $\tilde{\rho}l_c^{1-d}$ where $\tilde{\rho}$ is a dimensionless number of fiber segments in a unit volume, we have $\tilde{\mathcal{U}} = \tilde{\rho}\langle\hat{\mathcal{H}}_j(\gamma,\tilde{\kappa})\rangle_s$. Successively differentiating Eq. (4) with respect to γ, one obtains $\sigma = \frac{\partial\mathcal{U}}{\partial\gamma} = \mu\rho\tilde{\sigma}(\gamma,\tilde{\kappa})$ and $K = \frac{\partial\sigma}{\partial\gamma} = \mu\rho\tilde{K}(\gamma,\tilde{\kappa})$.

In our simulations, the line density ρ is specific to the chosen network architecture. In the lattice-based networks, we have $\tilde{\rho}_{2D} = \frac{6p}{\sqrt{3}}$ and $\tilde{\rho}_{3D} = \frac{12p}{\sqrt{2}}$ (see Appendices). With $l_c = l_0$ in lattice-based networks, the line density can be easily calculated for any given bond dilution probability q (see Appendices). For the off-lattice Mikado network, one can also define an average distance l_c between crosslinks. However, one does not need to know l_c explicitly to calculate the line density ρ_M of a Mikado network: $\rho_M = \tilde{\rho}_M/L$, where $\tilde{\rho}_M = nL^2$ and n is the number of fibers per unit area [51]. The line density ρ is thus explicitly known for lattice and off-lattice models and, as we show below, can be used to draw a quantitative comparison between the two computational approaches. It also follows that comparison between simulation results and experiments is possible by accounting for the line density $\tilde{\rho}$ of the specific network architecture. In particular, any measured quantity X (e.g., stress or modulus) must be compared as $\frac{X}{\mu l_c^{1-d}} = \tilde{\rho}\tilde{X}(\gamma,\tilde{\kappa})$, or as $\frac{X}{\mu L^{1-d}} = \tilde{\rho}_M\tilde{X}(\gamma,\tilde{\kappa})$ in the case of Mikado networks. Since $\tilde{\kappa}$ is dimensionless, different network architectures for a fixed connectivity z can be characterized by their respective $\tilde{\rho}$.

For 3D networks, the dimensionless fiber rigidity $\tilde{\kappa}$ is also related to the material concentration in a biopolymer network through the volume fraction of rods. For any given network structure of stiff rods, a cylindrical segment of length l_c and cross-section πa^2 occupies a volume fraction $\phi = \pi a^2\rho \propto a^2/l_c^2$. Since the fiber rigidity $\tilde{\kappa} = \kappa/\mu l_c^2 \sim a^2/l_c^2$, we obtain $\tilde{\kappa} \propto \phi$. Indeed, it has been shown that reconstituted collagen network mechanics is consistent with a reduced fiber rigidity $\tilde{\kappa}$ that is proportional to the protein concentration [26,27].

To explore the elastic response of the network, the volume-preserving simple shear strain γ is increased in steps over a range that covers all elastic regimes, typically from 0.1 to 1000%. At each $\delta\gamma$ strain step, the total elastic energy density is minimized by relaxing the internal degrees of freedom using a conjugate gradient minimization routine [52]. Lees-Edwards boundary conditions [53] ensure that the lengths of segments crossing the system boundaries are calculated correctly. From the minimized total elastic energy density, the shear stress σ and differential shear modulus K are evaluated. We also determine the normal stress $\tau = \frac{\partial\mathcal{U}}{\partial\varepsilon}|_\gamma$ where ε is a small uniform deformation applied normal to the shear boundaries. Measuring these quantities allows us to characterize the elastic regimes of the network which depends on the rigidity of the constituent fibers, the average density of crosslinks, as well as the applied deformation.

One can immediately identify different elastic regimes from the stiffening curves in Fig. 1(a): (i) a linear regime at low strain for which $K = G$ is constant and (ii) a nonlinear regime showing a rapid increase of K for $\gamma \gtrsim \gamma_0$ where γ_0 is the strain at the *onset* of nonlinearity. For networks with longer fibers and higher L/l_c, the strain γ_0 shifts to lower values. The linear modulus G reveals two distinct regimes as shown in the inset: (1) a bend-dominated regime with $G \sim \tilde{\kappa}$ and (2) a stretch-dominated regime at high $\tilde{\kappa}$, where bending is suppressed and the response is primarily due to stretching, i.e., $G \sim \mu$. Finally for large strains $\gamma \gtrsim \gamma_c$, which is the *critical* strain for which a fully floppy $\kappa = 0$ network develops rigidity, the stiffness grows independently of $\tilde{\kappa}$ as stretching modes become dominant. Here, the stiffening curves converge to that of the $\kappa = 0$ limit. This convergence is indicative of the ultimate dominance of stretching modes over bending for strains above γ_c (see Sec. IV).

Interestingly, we find that the characteristic features of stiffening are remarkably insensitive to local geometry (i.e., Mikado versus lattice based) and even dimensionality, for networks with the same average connectivity z. This holds, however, only below the respective isostatic thresholds, which are different in two and three dimensions. Specifically, we show in Fig. 1(b) that 2D Mikado and 2D lattice-based networks of the same z show even quantitative agreement, once we account for the difference in fiber density $\mu\tilde{\rho}$. By simply rescaling the stiffness with $\tilde{\rho}$, it seems that any explicit dependence of stiffness on the local geometry is factored out. Figure 1(c) shows a similar insensitivity to dimensionality, again accounting for network density $\tilde{\rho}$. This is even more apparent when plotting the normalized linear modulus $G/\tilde{\rho}$ versus $\kappa/\mu l_c^2$ with the actual l_c for 2D and 3D lattices, as shown in the inset to Fig. 1(c). As noted in Sec. (II A), we defined the reduced bending rigidity $\tilde{\kappa} = \kappa/(\mu\ell_0^2)$ for lattice-based networks, although the average distance l_c between crosslinks is somewhat larger than the lattice spacing ℓ_0 by the construction of our 2D lattice-based networks. Taking
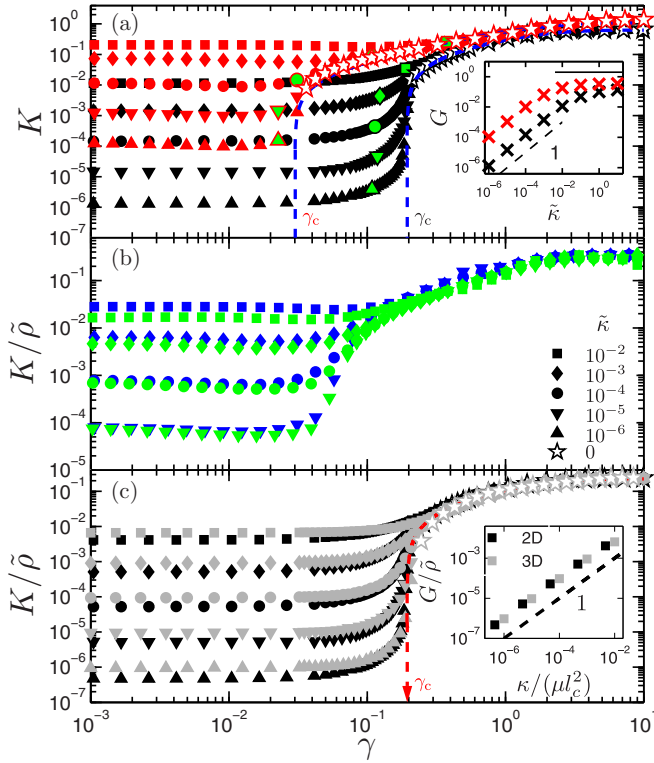
FIG. 1. (a) Stiffness K of a 2D lattice-based network as a function of the macroscopic strain γ. The black data correspond to $L/l_c = 3$ ($z = 3.2$) while the red data are for $L/l_c = 9$ ($z = 3.8$). In both cases, the stiffness is constant for low γ. At the onset of nonlinear stiffening marked by green symbols, K increases rapidly until $\gamma = \gamma_c$, defined in the limit of $\tilde{\kappa} = 0$ (blue dashed curves). For $\gamma \gg \gamma_c$, all curves collapse as stiffening is independent of $\tilde{\kappa}$ and dominated by fiber stretching. The strain γ_0 at the onset of nonlinearity shifts to lower strains with increasing L/l_c. Inset: The linear modulus G plotted as a function of fiber rigidity $\tilde{\kappa}$ also shows two elastic regimes: $G \sim \tilde{\kappa}$ (dashed line of unit slope) and $G \sim \tilde{\kappa}^0$ (solid horizontal line). Symbol colors represent the same L/l_c values in the main plot. (b) 2D Mikado (green data, $L/l_c = 11$, $z = 3.6$) and 2D lattice-based (blue data, $L/l_c = 6$, $z = 3.6$) network simulations normalized by their respective $\tilde{\rho}$, show the same qualitative behavior. (c) Stiffening curves from 3D (gray data) and 2D (black data) lattice-based networks, both with $z = 3.2$ show the same qualitative behavior as well as the same γ_c. The 3D and 2D data are each normalized by $\tilde{\rho}_{3D}$ and $\tilde{\rho}_{2D}$. Inset: For the same $z = 3.2$, the normalized linear modulus $G/\tilde{\rho}$ in 2D networks becomes virtually indistinguishable from 3D networks when plotted vs $\kappa/\mu l_c^2$, using the average distance l_c between crosslinks, i.e., $l_c \simeq 1.4\ell_0$ in 2D networks and $l_c = \ell_0$ in 3D networks.

the actual values of l_c for 2D ($\simeq 1.4\ell_0$) and 3D (ℓ_0) networks at the same $z = 3.2$, one obtains an almost perfect collapse of the data. Moreover, for the same connectivity (< 4), even the strain thresholds γ_0 and γ_c agree between Mikado and 2D lattice-based networks, and between 2D and 3D lattice-based networks [26,27].

III. LINEAR REGIME

The linear regime is characterized by a constant modulus G over the range of $\gamma < \gamma_0$. As mentioned above and shown in the inset of Fig. 1(a), the linear modulus exhibits two distinct

regimes: a bend-dominated one in which $G \sim \tilde{\kappa}$ and one in which G is independent of $\tilde{\kappa}$ and is a stretch-dominated regime where $G \sim \mu$. The crossover between the two regimes has been shown to be governed by a nonaffinity length scale λ_{NA}, which is determined by l_c, l_b as follows [35,36,42]:

$$\lambda_{NA} = l_c \left(\frac{l_c}{l_b} \right)^\zeta. \tag{5}$$

The exponent ζ depends on the network structure and the ratio L/λ_{NA} determines the crossover between the elastic regimes as

$$\frac{G}{G_{AFF}} \sim \left(\frac{L}{\lambda_{NA}} \right)^{2/\zeta}, \tag{6}$$

where G_{AFF} is the modulus in the affine limit. In our lattice-based networks, $G_{AFF} \sim \mu \ell_0^{1-d}$. For $\lambda_{NA} \geqslant L$, the modulus is governed by bending modes in the network. On the other hand for $\lambda_{NA} < L$, the modulus is governed by stretching modes.

Using mean-field arguments, [36] found that $\zeta \simeq 2/5$ for off-lattice 2D Mikado networks, while for 3D fcc lattice-based networks [42] found that $\zeta = 1$. Here, we focus on 2D lattice-based networks and show that $\zeta = 1$, as for the 3D fcc-based networks in [42]. In Fig. 2(a), we show G/G_{AFF} versus L/λ_{NA}. As can be seen, data obtained for different values of L/l_c collapse on a master curve with slope $2/\zeta = 2$. Significant deviation from the master curve is seen for data corresponding to relatively small values of L/l_c. This has been observed in a previous study on 3D fcc networks where such is attributed to a different scaling for networks in the vicinity of the rigidity percolation regime [42]. However, on replacing L by ($L - L_r$), where $L_r \approx 2.94$ is the average fiber length at rigidity percolation, we obtain an excellent collapse for all values of L/l_c with slope $2/\zeta = 2$ [Fig. 2(b)]. It follows from the above correction that in the linear regime $G/G_{AFF} \sim \kappa(L - L_r)^2$ as shown in the inset of Fig. 2(b). The scaling $G/G_{AFF} \sim \kappa L^2$ is known for 3D fcc lattice-based networks for $L \gg L_r$ [42]. Interestingly, such scaling behavior has been observed in experiments on hydrogels [54]. As we show above, the same scaling holds in 2D lattice-based networks.

With $\zeta = 2/5$, the modulus of off-lattice Mikado networks can be quantitatively captured by Eq. (6) [35,36]. The mean-field argument implicitly assumes that the nonaffinity length scale is larger than the bending correlation length which is given by

$$\lambda_b = l_c \left(\frac{l_b}{l_c} \right)^\zeta. \tag{7}$$

Moreover, both λ_{NA} and λ_b are assumed to be larger than l_c. It has been previously pointed out that in the limit of very flexible rods or for low concentrations Eq. (7) would predict $\lambda_b < l_c$, which is an unphysical result [36]. Thus when l_b/l_c becomes very small, by fixing $\lambda_b = l_c$, one obtains $\zeta = 1$ and $\lambda_{NA} = l_c^2/l_b$. Since the nonaffinity length scale obtained under the assumption of $\lambda_b = l_c$ is the same as found in lattice-based 2D and 3D networks, it seems that indeed the bending correlation length is very close to l_c. One does not expect this to hold for L approaching L_r where highly nonaffine deformations would include bending that occurs on length scales much larger than l_c. However, as we show above, by making an empirical
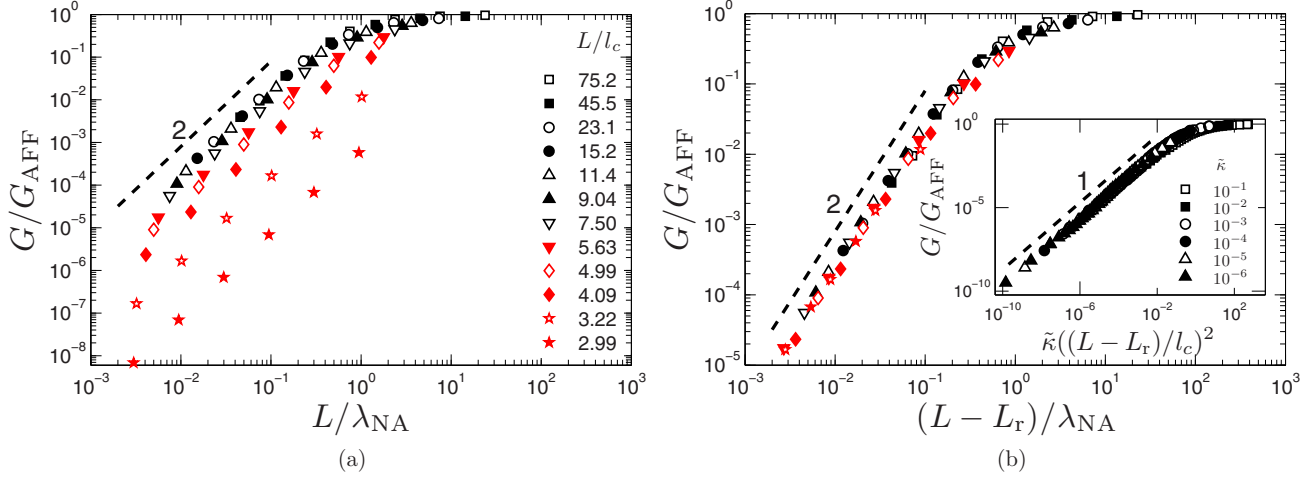
FIG. 2. Collapse of linear modulus with nonaffinity length scale (a) without and (b) with L_r correction. Red symbols represent networks in the vicinity of the rigidity percolation regime. The inset of (b) shows the collapse of the linear modulus with $\tilde{\kappa}(L - L_r)$.

correction to the length, i.e., replacing L by $(L - L_r)$, the scaling Eq. (6) is extended all the way up to the minimum length L_r required for rigidity percolation.

As shown above, the primary difference between the two types of network structures, lattice and off-lattice, is in their bending correlation length. However, with appropriately chosen exponent ζ, the linear modulus from both off-lattice and lattice-based networks can be quantitatively captured by Eq. (6). Thus, we conclude that Eqs. (5) and (6) give a unified description of the linear mechanics of fibrous networks independent of the detailed microstructure. In the next section, we focus on the stiffening regime, $\gamma_0 \leqslant \gamma \leqslant \gamma_c$. We demonstrate that independent of the details of the network, the nonlinear mechanics can also be described in a unified way.

IV. NONLINEAR REGIME

The shear and normal stresses are shown in Fig. 3(a). In the linear regime, σ is linear in strain while τ is always negative and quadratic as expected from symmetry arguments [21–24]. The negative sign in the normal stress is characteristic of biopolymer gels and has been observed in experiments [22], where it was attributed to the asymmetric thermal force-extension curve of the constituent fibers [55] or to nonaffine deformations of athermal networks [56–58], which lead to an effective network-level asymmetry in the response [23,24]. For very low strains, $\sigma \sim \gamma$ and $-\tau \sim \gamma^2$. As γ increases, the shear and normal stresses become increasingly comparable in magnitude. We define γ_0 as the strain at which $|\sigma| = |\tau|$, above which both stresses rapidly increase as the strain approaches γ_c. For $\gamma > \gamma_c$, both stress curves converge to their respective $\kappa = 0$ limits similarly observed for the K versus γ curves in Fig. 1. In the large strain limit, the shear response is again linear in strain, while the normal response approaches a constant.

An interesting feature of the strain stiffening regime can be observed in the K versus σ curves shown in Fig. 3(b), which reveal two distinct nonlinear stiffening regimes: a bend-dominated stiffening initiated by the points (σ_0, K_0) at the onset strain γ_0 which proceeds to stiffen as $K \sim \sigma^\alpha$, with α increasing for decreasing $\tilde{\kappa}$ [lower inset of Fig. 3(b)]; and a

stretch-dominated stiffening where all curves converge to $K \sim \sigma^{1/2}$ [24,41,59]. These results are consistent with previous theoretical work showing an evolution of exponents from $\alpha \simeq 1/2$ through 1 and higher values with decreasing $\tilde{\kappa}$ [41]. Such an evolution of the stiffening exponent with fiber rigidity is also consistent with recent experiments on collagen networks [26]. In contrast to what has been proposed in [60,61], however, our results show that there is no unique exponent $\alpha = 3/2$ in the initial stiffening regime.

A. Onset of strain stiffening

As mentioned above, the strain γ_0 at the onset of stiffening is characterized by the points of stiffness K_0 scaling linearly with shear stress σ_0. This feature can be understood as follows. At low stresses, the elastic energy density is dominated by soft bending modes and therefore $G \sim \tilde{\kappa}$ (Fig. 1, inset) [62,63]. Moreover, these networks stiffen at an onset stress σ_0 proportional to $\tilde{\kappa}$ [Fig. 3(a), inset], which coincides with the onset of fiber buckling [24,38]. From these observations, together with the fact that K and σ have the same units, it follows that $K_0 \approx G$ and σ_0 should depend in the same way on network parameters. Thus, the points (σ_0, K_0) should exhibit a linear relationship, as seen in networks for $\tilde{\kappa} \lesssim 10^{-2}$, which means that in these bend-dominated networks the onset strain $\gamma_0 \sim \sigma_0/K_0$ is independent of $\tilde{\kappa}$ [inset, Fig. 3(b)]. The independence of γ_0 on material parameters such as fiber rigidity or concentration suggests that there is no intrinsic length scale besides l_c that governs the response in the stiffening regime. This $\tilde{\kappa}$-independent regime is fully describable by a network of floppy ropelike fibers, and can be captured by our $\tilde{\kappa} = 0$ limit. In what follows, we will first derive the onset of nonlinear stiffening in this limit using pure geometric relaxation arguments to obtain $\gamma_0 \to \gamma_g$. We then build up from this result to obtain a generalized γ_0 for networks of finite $\tilde{\kappa}$.

Stiffening should therefore be understood in purely geometric terms as follows. In a network with bend-dominated linear elastic response, any fiber can relax its stored stretching energy by inducing bend amplitudes to the fiber strands
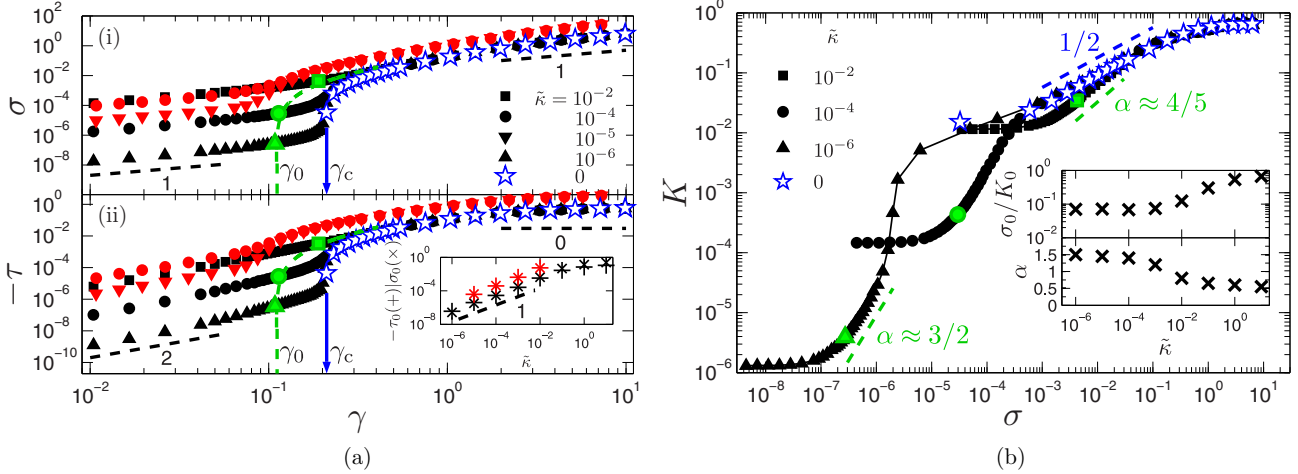
(a)

(b)

FIG. 3. (a) Shear stress σ (i) and negative normal stress $-\tau$ (ii) as a function of γ and $\tilde{\kappa}$ in a 2D lattice with $L/l_c = 3$, $z = 3.2$. In the linear regime, $|\sigma| \sim \gamma$ and $|\tau| \sim \gamma^2$. The stresses at the onset strain γ_0 of stiffening are indicated by green symbols interpolated by the green dashed schematic curve. The blue arrow marks the critical strain γ_c. Red data are from the Mikado simulation with $L/l_c = 11$, $z = 3.6$. Inset: At the onset of stiffening, $-\tau_0 \approx \sigma_0$, where both scale linearly with $\tilde{\kappa}$. (b) Stiffness K as a function of shear stress σ for different $\tilde{\kappa}$ in the 2D lattice. The lines connecting the data points only serve as visual guides. The green points correspond to (σ_0, K_0) at γ_0 and are replotted in the inset (upper panel) for all $\tilde{\kappa}$. Networks first undergo $K \sim \sigma^\alpha$ stiffening (green dashed lines) followed by $K \sim \sigma^{1/2}$ (blue dashed line). The lower panel of the inset shows the evolution of the stiffening exponent α with fiber rigidity.

directly connected to it (Fig. 4). When a strand f_i undergoes a backbone relaxation γL, it induces on strand f_j a transverse displacement $\delta'L \sim \gamma L$ and a longitudinal displacement (i.e., end-to-end contraction) $\delta''\ell$, both related as $\delta''\ell \approx \delta'L^2/l_c$
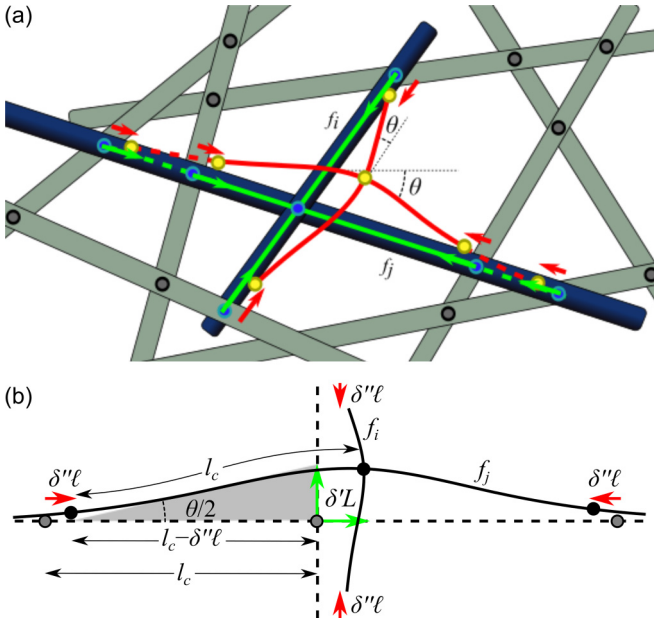

(a)

(b)

FIG. 4. (a) Schematic showing two interacting fiber strands f_i and f_j before (green) and after (red) relaxation. Circles denote points of mechanical constraints also shown before (blue) and after (yellow) relaxation. The backbone relaxation $\delta'L$ of f_i (green arrows) induces bending angles θ and longitudinal displacements $\delta''\ell$ (red arrows) on f_j, and vice versa. (b) A simplified diagram of the interacting strands before (dashed lines) and after (solid curves) relaxation shows the geometric relation between the coupled displacements $\delta'L$ and $\delta''\ell$ (gray triangle).

for small relaxations. These displacements are coupled since the longitudinal contraction of f_j relaxes the stretching energy which it would have acquired from the transverse bending displacement. Similarly, the backbone relaxation of f_j induces the same coupled displacements on f_i. To a first approximation, the total contraction of a fiber is given by the sum $\delta''L = \sum_{l_c}^{L} \delta''\ell \approx (\frac{L}{l_c})\delta''\ell \sim \gamma^2 L^3/l_c^2$. For an isotropic network, the maximum strain γ_g at which the displacements are purely governed by these *geometric* relaxations is when $\delta''L \approx \delta'L$. This maximum strain sets the onset of stiffening for floppy networks:

$$\gamma_0 \xrightarrow{\tilde{\kappa} \to 0^+} A\left(\frac{l_c}{L}\right)^2 \equiv \gamma_g, \qquad (8)$$

where $A \approx 1$. This result shows that the onset of stiffening in floppy networks is determined by the crosslinking density L/l_c. Indeed, if there are on average few mechanical constraints attached to a fiber, the network can be deformed over a greater range where geometric relaxations can be explored.

In the linear regime where fiber relaxations mainly induce bending displacements $\theta \sim \delta'L/l_c$, the elastic energy of the network should be dominated by fiber bending $\mathcal{H}_0^{(b)} \sim \frac{\kappa}{l_c}(\frac{\delta'L}{l_c})^2$. However, we have seen from the above geometric picture that longitudinal displacements $\delta''L$ couple to the transverse displacements. This higher order contribution to the bending displacement is taken into account as $\theta \sim \frac{\delta'L}{l_c} + \frac{\delta''L}{l_c}$ such that

$$\mathcal{H}_0^{(b)} \sim \frac{\kappa}{l_c}\left(\frac{\gamma L}{l_c} + \frac{\gamma^2 L^3}{l_c^3}\right)^2. \qquad (9)$$

One recovers Eq. (8) when higher order contributions to θ become significant. This suggests that the onset of stiffening γ_0 is not characterized by the dominance of stretching modes in the total energy. This is in contrast to earlier studies in
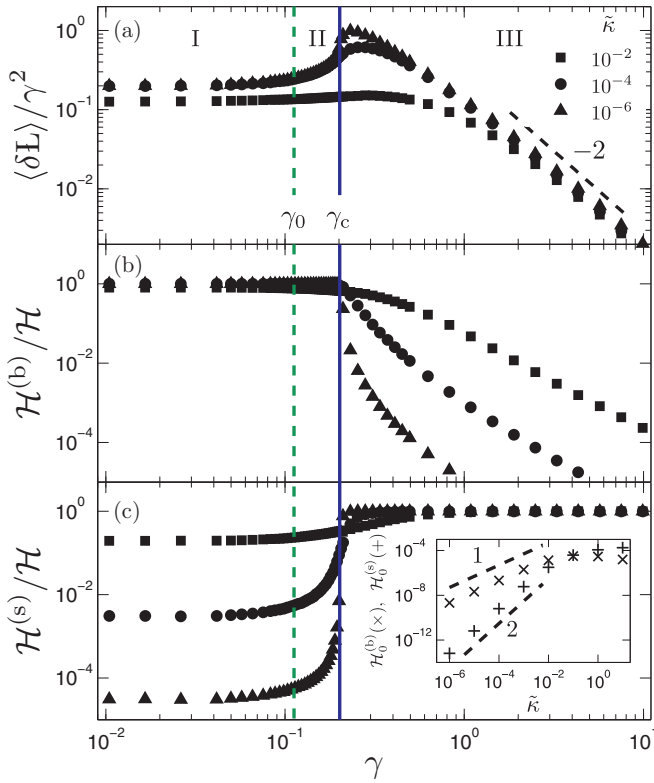
FIG. 5. (a) Average fiber excess length normalized by γ^2 vs strain. The linear regime and two stiffening regimes are indicated as I, II, and III, respectively. (b) Relative contributions of bending energy to the total elastic energy of the network vs strain and fiber rigidity. In regimes I and II, the total energy is dominated by bending contributions. (c) Stretching contributions become important only at strains $\gamma > \gamma_c$ (III). Inset: In the linear regime, $\mathcal{H}_0^{(b)} \sim \tilde{\kappa}$ in networks with bend-dominated linear elasticity while $\mathcal{H}_0^{(s)}$ shows a quadratic $\tilde{\kappa}$ dependence.

which the onset of nonlinearity was attributed to a transition from bending- to stretching-dominated behavior [38].

The contribution of higher order bending amplitudes should correspond to a rapid increase in *excess lengths*, so called because it is a length over which one can pull an undulated fiber without stretching its backbone. For a fiber strand with contour length l_c and local end-to-end length l (i.e., distance between adjacent crosslinks), we define the excess length as

$$\delta\text{Ł} = \begin{cases} \delta''\ell \sim \delta' L^2/l_c, & l < l_c. \\ 0, & l \geqslant l_c. \end{cases} \quad (10)$$

As bending amplitudes develop on the strands with increasing γ, excess lengths build up as γ^2 in the linear regime. We have verified this from our simulations [Fig. 5(a)]. Indeed, the linear regime (I) shows $\langle\delta\text{Ł}\rangle/\gamma^2 \sim$ const., followed by a rapid buildup near γ_0 (II) which peaks at γ_c. For $\gamma \gg \gamma_c$, the average excess length saturates to a constant (III), as one might expect for a network of stretched fibers.

The relative contributions of bending and stretching energy to the total elastic energy are shown in Figs. 5(b) and 5(c). As can be seen in both the linear (I) and the first stiffening (II) regimes, the total energy is dominated by fiber bending. We assume that any remaining stretching energy in a fiber strand

should scale as $\mathcal{H}_0^{(s)} \sim \mu l_c \epsilon_r^2$ in the linear regime, where ϵ_r is some small residual strain which we shall now determine self-consistently. The bending energy in the linear regime scales accordingly as $\mathcal{H}_0^{(b)} \sim \frac{\kappa}{l_c}(\frac{(\gamma - \epsilon_r)L}{l_c})^2$. Minimizing the total energy, we obtain $\epsilon_r = \frac{\mathcal{L}^2}{1+\mathcal{L}^2}\gamma \approx \gamma\mathcal{L}^2$, where $\mathcal{L} \equiv (l_b L)/l_c^2 \ll 1$ for floppy networks. The stretching and bending energies stored in the fiber strand can now be obtained in the linear regime to leading order as

$$\mathcal{H}_0^{(s)} \sim \mu l_c \epsilon_r^2 \approx \frac{\kappa^2 L^4}{\mu l_c^7}\gamma^2, \quad (11)$$

$$\mathcal{H}_0^{(b)} \sim \frac{\kappa}{l_c}\left(\frac{(\gamma - \epsilon_r)L}{l_c} + \frac{(\gamma - \epsilon_r)^2 L^3}{l_c^3}\right)^2 \approx \frac{\kappa L^2}{l_c^3}\gamma^2. \quad (12)$$

Both energy contributions scale quadratically with strain in the linear regime and are confirmed by our simulations [Figs. 5(b) and 5(c)]. Furthermore, the stretching contribution in floppy networks is highly suppressed because of the strong κ^2 dependence [inset, Fig. 5(c)]. This is in contrast to what has been pointed out in a previous study [42] that $\mathcal{H}_0^{(s)} \sim \mu\gamma^4 L^4/l_c^3$. In the case of networks with finite fiber rigidity, then Eq. (12) dictates that at the onset of stiffening $\gamma = \gamma_0$, when the higher order bending term becomes comparable to the linear term, we have

$$\gamma_0 \simeq \gamma_g + B\tilde{\kappa}, \quad (13)$$

where $B \approx 28$. In the asymptotic floppy network limit where $\tilde{\kappa} \to 0$, the onset of stiffening γ_0 is determined purely by γ_g [Eq. (8)] as shown in Fig. 6(a). This floppy limit is indicated by the finite range in $\tilde{\kappa}$ over which γ_0 is constant [Fig. 6(b)]. Indeed, the data from networks with different L/l_c show a good collapse of Eq. (13) [Fig. 6(c)]. We note here that for large values of $\tilde{\kappa}$ the onset of nonlinearity should be dictated by the affine limit at which such rigid fibers are aligned with a 45° angle corresponding to 100% strain. Indeed, Figs. 6(b) and 6(c) show that the onsets of stiffening in networks of rigid rods saturate to $\gamma_0 \to 1$.

B. Stress-controlled stiffening

Three key points that characterize network stiffening in regime II of Fig. 5 are (i) bending modes still dominating fiber stretching since the onset of nonlinearity is not a bend-stretch transition, (ii) nonlinear buildup of excess lengths, and (iii) normal stress being negative and comparable in magnitude to the shear stress. To understand the latter, consider the mean-field representation of the network in Fig. 7. Treating the fibers as bendable rods, every rod exerts a force of magnitude $F \propto \mu\epsilon_r$ on an arbitrary xz plane parallel to the shear boundary. In the floppy network limit, the forces parallel and normal to the plane are $F_\parallel \sim \frac{\kappa L}{l_c^4}(\delta' L + \delta'' L + \ldots)_\parallel$ and $F_\perp \sim \frac{\kappa L}{l_c^4}(\delta' L + \delta'' L + \ldots)_\perp$, where other higher order relaxations can be taken into account. The contribution from the connected fiber segments a and b to the shear and normal stresses are, respectively, $\sigma \approx (F_a + F_b)_\parallel/l_c^{d-1}$ and $\tau \approx (F_a + F_b)_\perp/l_c^{d-1}$ (see Appendices). Using the expressions for the force components including higher order corrections (see Appendices) and taking into account the appropriate signs relative to the
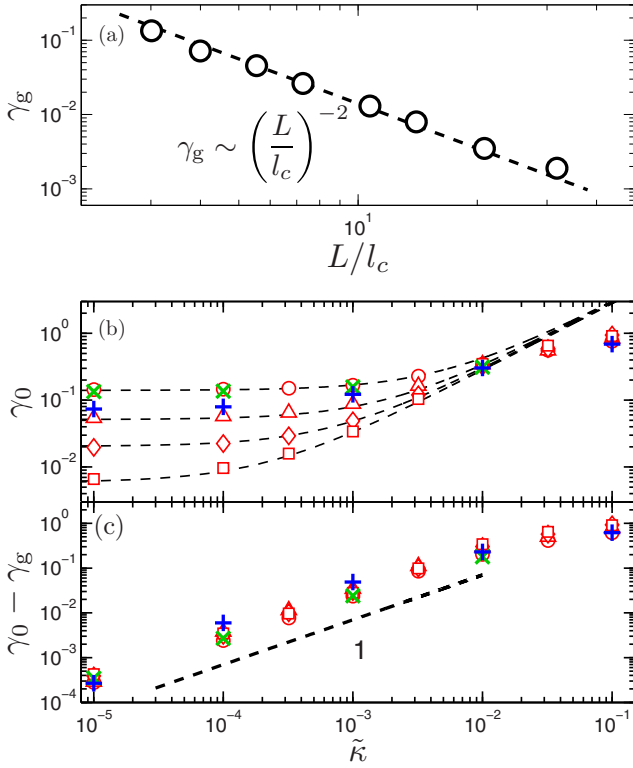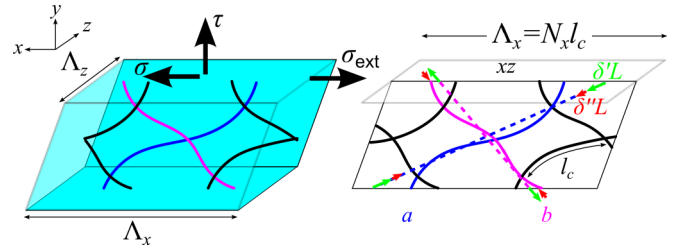
FIG. 7. On the left is a schematic of the sample with the shear σ and normal τ stresses acting on the xz plane. Bold arrows indicate the stresses. The coordinates are chosen such that the internal shear stress in response to the applied external shear stress σ_{ext} is positive. On the cutaway view shown at the right, the dashed lines represent fibers before relaxation while solid curves represent the fibers after they have undergone the coupled relaxations $\delta'L$ (green arrows) and $\delta''L$ (red arrows). The lateral sample dimensions Λ_x and Λ_z can be expressed in terms of the periodicity N_x and N_z of fiber segments with typical spacing l_c.

FIG. 6. (a) The onset of nonlinear stiffening of a floppy network with $l_b/l_c \ll l_c/L$ shifts to lower strains with increasing L/l_c as predicted by Eq. (8). (b) Fiber rigidity dependence of (i) γ_0 for different L/l_c in a 2D lattice: $L/l_c = 3$ ($\circ$), $L/l_c = 6$ ($\triangle$), $L/l_c = 9$ ($\diamond$), $L/l_c = 15$ ($\square$). Also shown for comparison are results from a 3D lattice ($\times$) with $L/l_c \approx 3$ and 2D Mikado ($+$) with $L/l_c \approx 11$. The dashed curves are a fit of Eq. (13). The constant level in the limit of $\tilde{\kappa} \to 0$ shows the value of γ_g predicted by Eq. (8). The onset strain γ_0 subsequently increases linearly with increasing $\tilde{\kappa}$ according to Eq. (13). (c) Collapse of the data from the upper panel using Eq. (13).

coordinate system shown in Fig. 7, we have

$$\sigma \approx \frac{\kappa L^2}{l_c^{d+3}}\gamma + \left(\frac{L}{l_c}\right)^2 \frac{\kappa L^4}{l_c^{d+5}}\gamma^3, \tag{14}$$

$$\tau \approx -\frac{\kappa L^4}{l_c^{d+5}}\gamma^2 - \left(\frac{L}{l_c}\right)^2 \frac{\kappa L^6}{l_c^{d+7}}\gamma^4. \tag{15}$$

Thus, for floppy networks at the onset of nonlinearity (i.e., $\gamma = \gamma_0 \simeq \gamma_g$) we obtain the result that $\sigma \approx |\tau| \sim \kappa/l_c^{d+1}$. Furthermore, taking $K = \frac{\partial \sigma}{\partial \gamma}$ in combination with $|\tau|$, we obtain the stiffening relation [26]:

$$K \simeq G + \chi|\tau|, \tag{16}$$

with linear modulus $G = \kappa L^2/l_c^{d+3}$ and the *susceptibility*

$$\chi = (L/l_c)^2 \sim \gamma_0^{-1}. \tag{17}$$

This indicates that the stiffness is dominated by $G \sim \kappa$ in the linear regime while the normal stresses provide additional stabilization in the nonlinear regime. Figure 8 shows the susceptibility to the normal stress as a function of the crosslinking density and fiber rigidity. The floppy network limit clearly shows the relation $\chi \sim \gamma_0^{-1}$.

To test the stiffening relation in Eq. (16), we compare K with $G + \chi|\tau|$ and plot them with σ shown in Fig. 9(a). Indeed, the linear regime is characterized by $G \sim \tilde{\kappa}$ where the magnitudes of the normal stresses are not significant compared to the shear stresses. In the stiffening regime, there is excellent agreement between K and $G + \chi|\tau|$. As can be seen in Fig. 9(a) data from the mikado network also follows the stiffening relation in Eq. (16). As in the case of lattice-based networks, the susceptibility of off-lattice networks to normal stress is the inverse of the stiffening strain. Since the stiffening strain depends on the network architecture, it appears that the stiffening relation in Eq. (16) together with a network architecture-dependent susceptibility comprises a general relation to describe the nonlinear stiffening of disordered elastic networks. As a final confirmation, we perform an additional relaxation of the networks by releasing the normal stresses. Indeed, when we relax the normal stresses, the stiffness drops to the level indicated by the linear modulus [Fig. 9(b)]. This is a clear indication that the normal stresses control the nonlinear
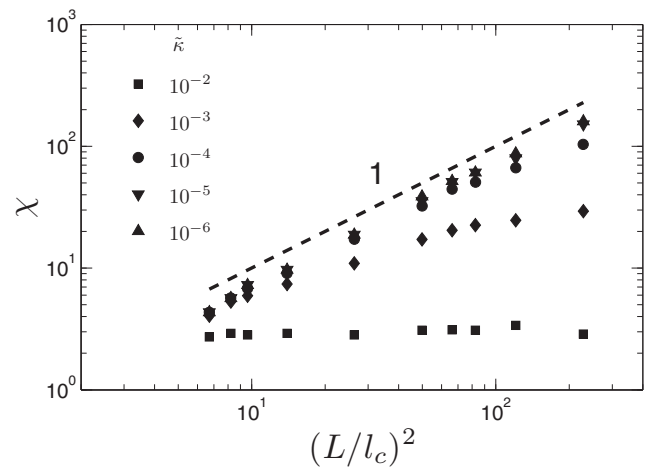

FIG. 8. Susceptibility to the normal stress in the nonlinear regime. As the fiber rigidity decreases, Eq. (17) is valid for increasingly larger range of L/l_c.
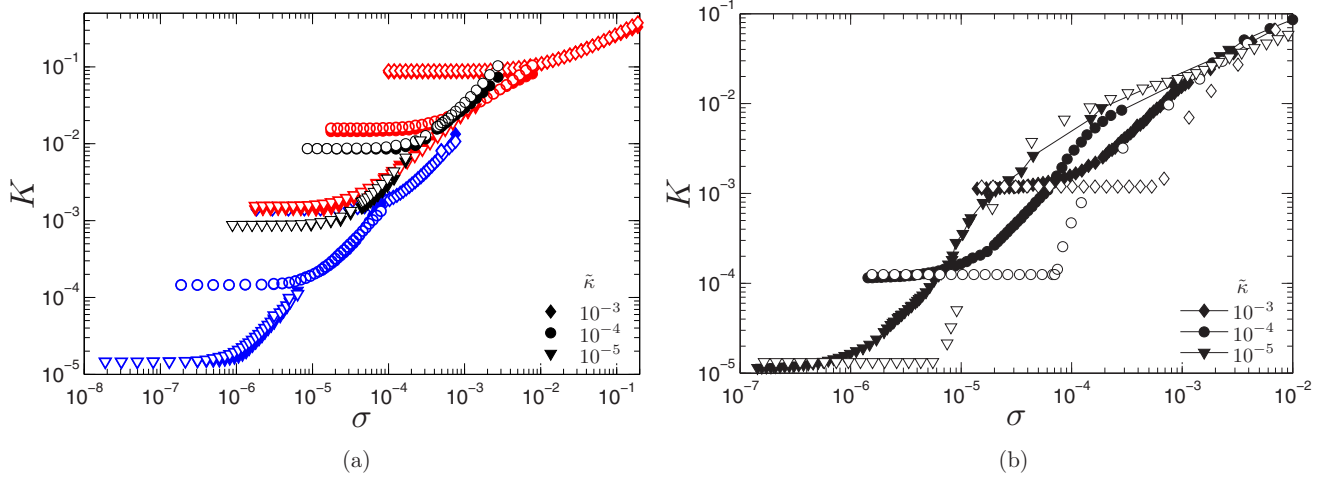
FIG. 9. (a) Stiffness vs shear stress (filled symbols) for a network with $L/l_c = 3$ (blue) and $L/l_c = 9$ (red) compared with the the stiffening hypothesis in Eq. (16) (empty symbols) show that normal stresses stabilize the bend-dominated nonlinear regime. Results from 2D Mikado simulations with $L/l_c = 11$ are shown in black. (b) Stiffness vs shear stress (filled symbols) for a network with $L/l_c = 3$. When the shear boundaries are relaxed, the stiffness drops to the level indicated by the linear regime (open symbols).

stiffening of these networks. Moreover, the onset of stiffening with free normal boundaries occurs near γ_c at the beginning of regime III in Fig. 5, which is also the regime where stretching dominates, as shown in that figure. Importantly, throughout the stiffening in regime II, the bending energy still dominates the stretching energy.

V. DISCUSSION

Here, we have studied the elastic behavior of subisostatic athermal fiber networks. Athermal fiber networks can be used to model the mechanics of biological networks such as collagen. It is *a priori* not clear whether one needs to take into account the detailed microstructure of a biological network in a computational model to capture the mechanics. Most of the computational studies are based on lattice-based [29,41–44] or off-lattice based network structures [24,34–36,38,39]. The primary advantage of a lattice-based approach is the computational efficiency. By contrast, off-lattice networks, though computationally intensive, would appear to be more realistic, in the sense that the network structure has built in spatial disorder that is a key feature of biologically relevant networks. Here we show that despite the structural differences these two approaches can be unified and are equally suited to describe most aspects of the mechanical response of athermal fiber networks. We show that the elastic modulus in the linear regime, for both lattice- and off-lattice-based networks, can be fully characterized in terms of a nonaffinity length scale λ_{NA} [35,36,42], which depends on the underlying network structure. The scaling relation in Eq. (6) with the network-dependent exponent ζ captures the crossover behavior of the linear modulus of a network. The nonaffinity length scale can be derived for a given filamentous network using mean-field arguments [35,36]. However, we show that with an empirical correction, replacing the filament length L by $L - L_r$, the scaling relation Eq. (6) can even capture the linear mechanics of networks close to the rigidity percolation where non-mean-field behavior is expected. Our computational approach is

based on networks which are composed of discrete filaments allowing for an unambiguous and intuitive definition of the nonaffinity length scale λ_{NA}. However, the concept of the nonaffinity length scale can be extended to branched networks by considering the average branching distance.

Previous computational studies on both lattice and off-lattice-based networks have reported that the transition from the linear to nonlinear regime under strain is marked by an initial softening of the modulus [24,38,64]. The softening occurs due to buckling of the filaments under compression. However, to our knowledge, experimental demonstration of the softening has remained elusive. We suggest that the buckling-induced softening is an artifact of simulations. We show that on introducing undulations in the discrete filaments no such softening is seen in the simulations (Fig. 10). Under compression, the undulating filaments undergo increased bending but do not buckle. It is expected that in any biological network the filaments exhibit undulations, either from defects or prestress, and hence would not demonstrate buckling-induced softening under strain.

The onset of the nonlinear regime is marked by a stiffening strain γ_0 at which the normal stress becomes comparable to the shear stress. We derive γ_0 using only geometric arguments and demonstrate that for bend-dominated networks our expression is in excellent agreement with the simulations. In a bend dominated network, with increasing strain, the bend amplitude increases. The increase in bend amplitude is coupled to the longitudinal contraction of the filament along its backbone. When these two displacements, namely, the contraction along the backbone and the bend amplitude, become comparable, nonlinear stiffening sets in such that any further strain induces stretching of filaments in addition to bending. We also demonstrate that the above geometric argument immediately leads to normal stress becoming comparable to the shear stress at γ_0. Obtaining γ_0 as the strain at which normal and shear stresses become equal provides an unambiguous definition of the onset of stiffening. Our derivation of γ_0 is purely geometrical and can be considered to hold only in the limit
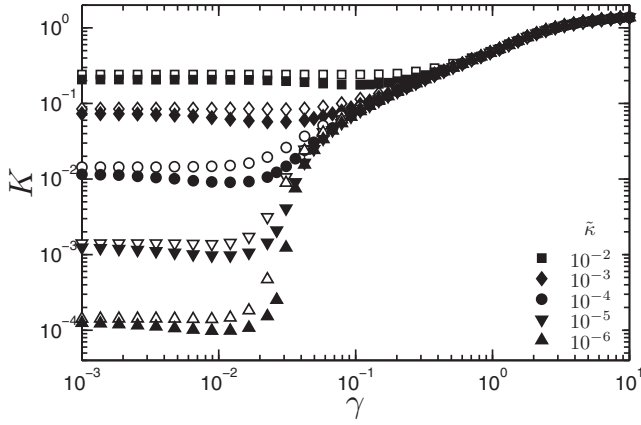
FIG. 10. For networks with high connectivity and crosslinking density such as in a 2D lattice with $z = 3.8$ and $L/l_c = 9$ [filled symbols are the red data set from Fig. 1(a)], an apparent "softening" of the network is observed as K dips slightly relative to G. This artifact is not present for lower z and L/l_c [black data set in Fig. 1(a)] or when undulations are introduced to the fibers (open symbols) by applying a small uniform macroscopic compressive strain ($\varepsilon < 1\%$) normal to the network boundaries.

of vanishing bending rigidity. We derive an expression for the stiffening strain for finite bending rigidity and show that it can accurately describe the onset of stiffening for even those networks which are not bend dominated in the linear regime. The onset of stiffening strain, as expected, reduces to γ_0 in the limit of vanishing bending rigidity. Experimental determination of γ_0 is based on an arbitrary criterion such as the strain at which the differential modulus becomes three times the linear modulus [26]. However, the advantage of defining γ_0 based on stress could be nullified in experiments due to the ambiguity in determining the normal stress. Any prestress in the network would offset the normal stresses generated in the network under strain.

In the nonlinear regime, for $\gamma > \gamma_0$ both bending and stretching energies increase faster than a quadratic dependence on the strain which manifests itself in a rapid increase in the modulus with strain. At a certain strain $\gamma_c > \gamma_0$, the two energies become comparable to each other. The nonlinear mechanics in the range $\gamma_0 \leqslant \gamma \leqslant \gamma_c$ are controlled by normal stress in the network. We show that the elastic modulus increases in proportion to the normal stress. The observation that the modulus scales linearly with the normal stress is reminiscent of the stabilization of floppy networks under normal stress. Fiber networks, in the absence of bending interactions, are floppy and can be stabilized by several fields [27–33] including normal stress. The normal stress can be generated internally by molecular motors [31,32] or externally by subjecting the network to a global deformation [65,66]. Independent of the origin of the normal stress, the linear modulus of an initially unstable network (in the absence of normal stress) scales linearly with the normal stress. Here, we generalize the idea of stabilization by normal stress to an initially stable network (finite bending interactions) in the nonlinear regime, where the normal stress becomes the dominant stress in the network and controls the stiffening. We present a scaling argument which yields a linear relation

between the nonlinear modulus and the normal stress in the stiffening regime. The modulus and the normal stress are related via the network susceptibility to the latter. We show that the susceptibility is fully governed by the underlying geometry of the network. In fact, the susceptibility scales as the inverse γ_0. To further test the role of normal stress in the stiffening regime, we consider a scenario in which normal stress is always relaxed to zero for any imposed shear strain by allowing the shear boundaries to retract along the normal direction. We observe that there is no stiffening in the absence of normal stress. The modulus remains clamped to the linear modulus in the regime $\gamma_0 \leqslant \gamma < \gamma_c$. Experiments on collagen networks have shown that over a wide range of collagen concentration K scales linearly with the shear stress σ [26,67]. We show that such dependence of K on the shear stress follows naturally from our hypothesis of normal stress-induced stiffening. Over a significant range of bending rigidity which is directly related to protein concentration [26], we find that the shear stress scales approximately linearly with the normal stress. It follows that stiffening can be understood in terms of normal stresses.

In summary, we study the mechanics of athermal fiber networks. The linear mechanics can be captured in terms of nonaffinity length scale. The nonlinear mechanics can be considered as composed of two regimes. From the onset of stiffening to a critical strain, the first regime, the stiffening is governed by strain-induced normal stresses. Beyond the critical strain, the stiffening is governed by stretching of filaments. Our study provides a general framework to capture linear and nonlinear mechanics of fiber networks for both lattice- and off-lattice-based network structures.

APPENDIX A: LINE DENSITY CALCULATION OF LATTICE-BASED NETWORKS

On any lattice with uniform bond lengths l_c, the line density can be calculated as the total length of bonds per unit volume, i.e., $\rho = n_b l_c / v_0$ where n_s is the number of bonds in a unit cell of volume v_0. In a two-dimensional diluted triangular lattice, a unit cell has each bond shared by two triangles, so that $n_s = \frac{3}{2} p$, where p is the probability that a bond exists. With $v_0 = \frac{\sqrt{3}}{4} l_c^2$, we obtain

$$\rho_{2D} = \frac{\frac{3}{2} p l_c}{\frac{\sqrt{3}}{4} l_c^2} = \frac{\tilde{\rho}_{2D}}{l_c}, \quad \tilde{\rho}_{2D} = \frac{6p}{\sqrt{3}}.$$

In the case of a 3D diluted fcc lattice, we can imagine six lines intersecting each vertex. Enclosing a vertex by a sphere of radius $l_c/2$, the total length of the enclosed bonds is $6p l_c$. Dividing by the volume of the sphere and multiplying by the

packing fraction of the fcc lattice which is $\pi/\sqrt{18}$, we have

$$\rho_{3D} = \frac{6pl_c}{\frac{4}{3}\pi\left(\frac{l_c}{2}\right)^3}\left(\frac{\pi}{\sqrt{18}}\right) = \frac{\tilde{\rho}_{3D}}{l_c^2}, \quad \tilde{\rho}_{3D} = \frac{12p}{\sqrt{2}}.$$

APPENDIX B: SHEAR AND NORMAL STRESSES ON A BOUNDARY DUE TO CONNECTED ELASTIC RODS

We use a mean-field scaling argument to derive the shear and normal stresses on the boundary of a sample under simple shear strain. Referring to Fig. 7, we assume that the fiber crossings are spaced at l_c and have a periodicity along the lateral boundaries N_x and N_z. Every fiber is an elastic rod with stretch modulus μ and bending rigidity κ. Each rod exerts a force of magnitude $F \propto \mu\epsilon_r \approx \frac{\kappa L^2}{l_c^4}\gamma$. The last approximation is when we take the floppy limit for the residual stretch ϵ_r. As derived in Sec. IV A, the lowest order backbone relaxations are $\delta'L \sim \gamma L$ and $\delta''L \sim \gamma^2 L^3/l_c^2$, so we can express F to first order as $F \sim \frac{\kappa L}{l_c^4}\delta'L$. In general if we include higher order fiber relaxations, we should be able to write

$$F \sim \frac{\kappa L}{l_c^4}(\delta'L + \delta''L + \delta'''L + \ldots).$$

We can calculate stresses by summing up the components parallel and perpendicular to the shear boundary of the forces due to the relaxations of the crossed fibers a and b. We take the lateral dimensions $\Lambda_x = N_x l_c$ and $\Lambda_z = N_z l_c$. In a 3D system, the shear and normal stresses are calculated by summing up the parallel and perpendicular components, respectively, of F along the shear boundary:

$$\sigma = \frac{\sum_{i\in x,z}\sum_j^{N_i}(F_a + F_b)_{\|j}}{\prod_{i\in x,z}\Lambda_i} \sim \frac{N_x N_z (F_a + F_b)_\|}{\Lambda_x \Lambda_z}$$

$$\approx (F_a + F_b)_\|/l_c^2,$$

$$\tau = \frac{\sum_{i\in x,z}\sum_j^{N_i}(F_a + F_b)_{\perp j}}{\prod_{i\in x,z}\Lambda_i} \sim \frac{N_x N_z (F_a + F_b)_\perp}{\Lambda_x \Lambda_z}$$

$$\approx (F_a + F_b)_\perp/l_c^2.$$

In a 2D system, these should easily translate to $\sigma \approx (F_a + F_b)_\|/l_c$ and $\tau \approx (F_a + F_b)_\perp/l_c$. We proceed to calculate the stresses in either $d = 2$ or 3 systems by substituting the force components:

$$\sigma \approx \frac{\kappa L}{l_c^{d+3}}[(\delta'L_a + \delta''L_a) + (\delta'L_b - \delta''L_b)]_\|,$$

$$\tau \approx \frac{\kappa L}{l_c^{d+3}}[(-\delta'L_a - \delta''L_a) + (\delta'L_b - \delta''L_b)]_\perp,$$

where the cancellation of terms come from the mean-field assumption on the relaxations leading to the result one obtains in the linear regime:

$$\sigma \sim \frac{\kappa L}{l_c^{d+3}}\delta'L \approx \frac{\kappa L^2}{l_c^{d+3}}\gamma,$$

$$\tau \sim -\frac{\kappa L}{l_c^{d+3}}\delta''L \approx -\frac{\kappa L^4}{l_c^{d+5}}\gamma^2.$$
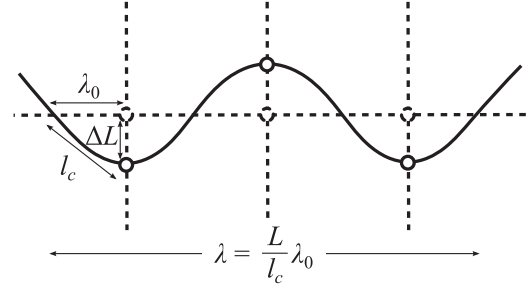

FIG. 11. Schematic of a fiber (dashed horizontal line) undergoing relaxation (solid curve). Other fibers are also shown with connections indicated by circles. The relaxed length is defined as λ in terms of the relaxed segment length λ_0.

Invoking symmetry properties of σ and τ, we generalize the above as

$$\sigma \sim \frac{\kappa L}{l_c^{d+3}}(\delta'L + \delta'''L + \ldots),$$

$$\tau \sim -\frac{\kappa L}{l_c^{d+3}}(\delta''L + \delta^{(iv)}L + \ldots).$$

We now obtain the higher order relaxation terms $\delta'''L$ and $\delta^{(iv)}L$. From the diagram shown in Fig. 11, we define the generalized bending amplitude $\Delta L \approx \delta'L + \delta''L$ and obtain the relaxed fiber length:

$$\lambda = L\left[1 - \left(\frac{\Delta L}{l_c}\right)^2\right]^{\frac{1}{2}}$$

$$\approx L - \frac{\gamma^2 L^3}{l_c^2} - \frac{\gamma^3 L^5}{l_c^4} - \frac{\gamma^4 L^7}{l_c^6} - \cdots.$$

The resulting length change of the fiber can now be written as

$$\Delta L = \delta'L + \delta''L + \delta'''L + \delta^{(iv)}L + \ldots$$

$$= \gamma L + \frac{\gamma^2 L^3}{l_c^2} + \frac{\gamma^3 L^5}{l_c^4} + \frac{\gamma^4 L^7}{l_c^6} + \ldots$$

such that

$$\delta'''L \sim \frac{\gamma^3 L^5}{l_c^4}, \quad \delta^{(iv)}L \sim \frac{\gamma^4 L^7}{l_c^6}.$$

Finally, we substitute these higher order relaxation terms into the generalized shear and normal stresses leading to

$$\sigma \approx \frac{\kappa L^2}{l_c^{d+3}}\gamma + \left(\frac{L}{l_c}\right)^2\frac{\kappa L^4}{l_c^{d+5}}\gamma^3,$$

$$\tau \approx -\frac{\kappa L^4}{l_c^{d+5}}\gamma^2 - \left(\frac{L}{l_c}\right)^2\frac{\kappa L^6}{l_c^{d+7}}\gamma^4.$$

[1] P. A. Janmey, Curr. Opin. Cell Biol. **3**, 4 (1991).

[2] D. H. Wachsstock, W. H. Schwarz, and T. D. Pollard, Biophys. J. **66**, 801 (1994).

[3] K. E. Kasza, A. C. Rowat, J. Y. Liu, T. E. Angelini, C. P. Brangwynne, G. H. Koenderink, and D. A. Weitz, Curr. Opin. Cell Biol. **19**, 101 (2007).

[4] A. R. Bausch and K. Kroy, Nat. Phys. **2**, 231 (2006).

[5] D. A. Fletcher and D. Mullins, Nat. Phys. **463**, 485 (2010).

[6] O. Chaudhuri, S. H. Parekh, and D. A. Fletcher, Nature (London) **445**, 295 (2007).

[7] R. Tharmann, M. M. A. E. Claessens, and A. R. Bausch, Phys. Rev. Lett. **98**, 088103 (2007).

[8] R. C. Picu, Soft Matter **7**, 6768 (2011).

[9] C. P. Broedersz and F. C. MacKintosh, Rev. Mod. Phys. **86**, 995 (2014).

[10] M. L. Gardel, J. H. Shin, F. C. MacKintosh, L. Mahadevan, P. Matsudaira, and D. A. Weitz, Science **304**, 1301 (2004).

[11] P. A. Janmey, E. J. Amis, and J. D. Ferry, J. Rheol. **27**, 135 (1983).

[12] J. Xu, Y. Tseng, and D. Wirtz, J. Biological Chemistry **275**, 35886 (2000).

[13] C. Storm, J. J. Pastore, F. C. MacKintosh, T. C. Lubensky, and P. A. Janmey, Nature (London) **435**, 191 (2005).

[14] B. A. DiDonna and A. J. Levine, Phys. Rev. Lett. **97**, 068104 (2006).

[15] M. L. Gardel *et al.*, Proc. Natl. Acad. Sci. USA **103**, 1762 (2006).

[16] B. Wagner *et al.*, Proc. Natl. Acad. Sci. USA **103**, 13974 (2006).

[17] A. Kabla and L. Mahadevan, J. R. Soc., Interface **4**, 99 (2007).

[18] K. E. Kasza, G. H. Koenderink, Y. C. Lin, C. P. Broedersz, W. Messner, F. Nakamura, T. P. Stossel, F. C. MacKintosh, and D. A. Weitz, Phys. Rev. E **79**, 041928 (2009).

[19] A. M. Stein, D. A. Vader, D. A. Weitz, and L. M. Sander, Complexity **16**, 22 (2011).

[20] H. Saraf, K. T. Ramesh, A. M. Lennon, A. C. Merkle, and J. C. Roberts, J. Biomechanics **40**, 1960 (2007).

[21] J. H. Poynting, Proc. R. Soc. A **82**, 546 (1909); **86**, 534 (1912).

[22] P. A. Janmey, M. E. McCormick, S. Rammensee, J. L. Leight, P. C. Georges, and F. C. MacKintosh, Nat. Mater. **6**, 48 (2006).

[23] C. Heussinger, B. Schaefer, and E. Frey, Phys. Rev. E **76**, 031906 (2007).

[24] E. Conti and F. C. MacKintosh, Phys. Rev. Lett. **102**, 088102 (2009).

[25] S. B. Lindström, D. A. Vader, A. Kulachenko, and D. A. Weitz, Phys. Rev. E **82**, 051905 (2010).

[26] A. J. Licup, S. Münster, A. Sharma, M. Sheinman, L. Jawerth, B. Fabry, D. A. Weitz, and F. C. MacKintosh, Proc. Natl. Acad. Sci. USA **112**, 9573 (2015).

[27] A. Sharma, A. J. Licup, R. Rens, M. Sheinman, K. A. Jansen, G. H. Koenderink, and F. C. MacKintosh, arXiv:1506.07792.

[28] M. Wyart, H. Liang, A. Kabla, and L. Mahadevan, Phys. Rev. Lett. **101**, 215501 (2008).

[29] C. P. Broedersz, X. Mao, T. C. Lubensky, and F. C. MacKintosh, Nat. Phys. **7**, 983 (2011).

[30] M. Dennison, M. Sheinman, C. Storm, and F. C. MacKintosh, Phys. Rev. Lett. **111**, 095503 (2013).

[31] M. Sheinman, C. P. Broedersz, and F. C. MacKintosh, Phys. Rev. Lett. **109**, 238101 (2012).

[32] Y. Shokef and S. A. Safran, Phys. Rev. Lett. **108**, 178103 (2012).

[33] J. Feng, H. Levine, X. Mao, and L. M. Sander, Soft Matter (2016).

[34] J. Wilhelm and E. Frey, Phys. Rev. Lett. **91**, 108103 (2003).

[35] D. A. Head, A. J. Levine, and F. C. MacKintosh, Phys. Rev. Lett. **91**, 108102 (2003).

[36] D. A. Head, A. J. Levine, and F. C. MacKintosh, Phys. Rev. E **68**, 061907 (2003).

[37] M. Das, F. C. MacKintosh, and A. J. Levine, Phys. Rev. Lett. **99**, 038101 (2007).

[38] P. R. Onck, T. Koeman, T. van Dillen, and E. van der Giessen, Phys. Rev. Lett **95**, 178102 (2005).

[39] E. M. Huisman, C. Storm, and G. T. Barkema, Phys. Rev. E **78**, 051801 (2008).

[40] A. Shahsavari and R. C. Picu, Phys. Rev. E **86**, 011923 (2012).

[41] C. P. Broedersz and F. C. MacKintosh, Soft Matter **7**, 3186 (2011).

[42] C. P. Broedersz, M. Sheinman, and F. C. MacKintosh, Phys. Rev. Lett. **108**, 078102 (2012).

[43] C. Heussinger and E. Frey, Phys. Rev. E **75**, 011917 (2007).

[44] X. Mao, O. Stenull, and T. C. Lubensky, Phys. Rev. E **87**, 042602 (2013).

[45] X. Mao, O. Stenull, and T. C. Lubensky, Phys. Rev. E **87**, 042601 (2013).

[46] M. Sheinman, C. P. Broedersz, and F. C. MacKintosh, Phys. Rev. E **85**, 021801 (2012).

[47] E. M. Huisman, T. van Dillen, P. R. Onck, and E. Van der Giessen, Phys. Rev. Lett. **99**, 208103 (2007).

[48] J. C. Maxwell, Philo. Mag. Series 4 **27**, 294 (1864).

[49] S. Alexander, Phys. Rep. **296**, 65 (1998).

[50] L. D. Landau and E. M. Lifshitz, *Theory of Elasticity*, 2nd ed. (Pergamon, Oxford, 1970), pp. 44–97.

[51] D. A. Head, F. C. MacKintosh, and A. J. Levine, Phys. Rev. E **68**, 025101(R) (2003).

[52] W. H. Press, S. A. Teukolsky, W. T. Vetterling, and B. P. Flannery, *Numerical Recipes in C: The Art of Scientific Computing*, 2nd ed. (Cambridge University, Cambridge, England, 1992).

[53] A. W. Lees and S. F. Edwards, J. Phys. C **5**, 1921 (1972).

[54] M. Jaspers, M. Dennison, M. F. J. Mabesoone, F. C. MacKintosh, A. E. Rowan, and P. H. J. Kouwer, Nat. Comm. **5**, 5808 (2014).

[55] F. C. MacKintosh, J. Käs, and P. A. Janmey, Phys. Rev. Lett. **75**, 4425 (1995).

[56] H. Hatami-Marbini and R. C. Picu, Phys. Rev. E **77**, 062103 (2008).

[57] T. van Dillen, P. R. Onck, and E. Van der Giessen, J. Mech. Phys. Solids **56**, 2240 (2008).

[58] A. Basu, Q. Wen, X. Mao, T. C. Lubensky, P. A. Janmey, and A. G. Yodh, Macromolecules **44**, 1671 (2011).

[59] G. A. Buxton and N. Clarke, Phys. Rev. Lett. **98**, 238103 (2007).

[60] G. Zagar, P. R. Onck, and E. Van der Giessen, Macromolecules **44**, 7026 (2011).

[61] G. Žagar, P. R. Onck, and E. Van der Giessen, Biophys. J. **108**, 1470 (2015).

[62] K. Kroy and E. Frey, Phys. Rev. Lett. **77**, 306 (1996).

[63] R. L. Satcher and C. F. Dewey, Jr., Biophys. J. **71**, 109 (1996).

[64] A. S. Abhilash, P. K. Purohit, and S. P. Joshi, Soft Matter **8**, 7004 (2012).

[65] H. E. Amuasi, C. Heussinger, R. L. C. Vink, and A. Zippelius, New J. Phys. **17**, 083035 (2015).

[66] K. M. Heidemann, A. Sharma, F. Rehfeldt, C. F. Schmidt, and M. Wardetzky, Soft Matter **11**, 343 (2015).

[67] Y. C. Fung, Am. J. Physiol. **213**, 1532 (1967).